

Combinatorial study of the Li-La-Zr-O system

*Ethan Anderson, Antranik Jonderian, Rustam Z. Khaliullin and Eric McCalla**

Department of Chemistry, McGill University, Montreal, Canada

*Corresponding author: eric.mccalla@mcgill.ca

Abstract: Lithium-stuffed garnets based on $\text{Li}_7\text{La}_3\text{Zr}_2\text{O}_{12}$ (LLZO) have attracted a lot of attention as candidate electrolytes for all-solid lithium batteries. Doping studies have shown that substitutions will induce lithium vacancies and convert the structure from tetragonal to cubic and greatly increase ionic conductivity. However, the impacts of structure and composition have not been fully decoupled. Herein, we systematically study over 700 samples from the Li-La-Zr-O composition space to produce phase stabilities over the entire pseudoternary for the first time. The results obtained for samples made at 900 °C show that the pyrochlore phase $\text{La}_2\text{Zr}_2\text{O}_7$, previously only known to exist at its formal composition in the Li-La-Zr-O system, is in fact part of a large lithium containing solid solution region extending well into the pseudoternary. Furthermore, the LLZO phase of highest interest is also a solid solution with the cubic phase representing a very small region on the lithium-deficient side of $\text{Li}_7\text{La}_3\text{Zr}_2\text{O}_{12}$ such that it is nearly impossible to synthesize the cubic phase in the Li-La-Zr-O system without the presence of the detrimental pyrochlore phase. We also show that the cubic phase here has only marginally higher bulk conductivity than the tetragonal phase, indicating that the structural change to cubic, though necessary, is not sufficient to yield the large improvements in conductivity seen in doping studies in the literature. We also demonstrate that secondary phases can help improve the grain boundary conductivity, as we reported previously in perovskite La-Li-Ti-O materials.

1. Introduction

Significant progress in battery performance has been made since the first commercialization of lithium ion batteries in 1990, but material improvements to lithium ion anodes have been minimal. Even 30 years later, the only widely utilized anode material remains graphite (though small amounts of silicon are now added) [1,2]. The ideal anode material would be metallic lithium, since it has the highest possible capacity and lowest redox potential, but conventional liquid organic electrolytes provide no resistance against lithium dendrite growth which can lead to internal short circuits and thermal runaway, thus posing an unacceptable safety risk [3–5]. Instead, the battery community has pursued solid electrolytes to enable the use of lithium metal anodes. Solid electrolytes primarily offer much greater resistance to lithium dendrite growth and are inherently safer than organic liquid electrolytes, which can vaporize and catch fire.

Among the many families of solid electrolytes currently being studied, metal oxide ceramics have attracted significant attention for their combination of high ionic conductivity, good electrochemical stability, air and moisture stability, and relative ease of manufacture [6,7]. Perovskite lithium lanthanum titanium oxide (LLTO) with compositions $\text{Li}_{3x}\text{La}_{2/3-x}\text{TiO}_3$ represent one example of a metal oxide solid electrolyte with these properties, and we have previously published a high-throughput exploration of the Li-La-Ti-O system in order to better understand these materials [8]. Motivated by the benefits from studying the entire LLTO system, here, we study the Li-La-Zr-O system in a similar manner, focusing on the lithium stuffed garnet $\text{Li}_7\text{La}_3\text{Zr}_2\text{O}_{12}$ (LLZO) which has been of high interest as a potential solid electrolyte.

LLZO materials have a combination of high lithium conductivity (as high as 2.06×10^{-3} S/cm when doped appropriately) [9] and stability in contact with lithium metal that make it one of the most attractive candidates for solid state batteries [10,11]. LLZO can take either a tetragonal

crystal structure (space group $I4_1/acd$) or a cubic crystal structure (space group $Ia-3d$), with cubic LLZO typically being 2 orders of magnitude more conductive to lithium [12]. It should be noted that the tetragonal and cubic phases have not been obtained at the same composition. The tetragonal phase is obtained for undoped LLZO, while a variety of dopants have given rise to the cubic phase. The difference in conductivity can therefore be explained by a combination of composition and structure. For example, the lithium sites in tetragonal LLZO are fully ordered and require concerted migration of lithium ions for conduction to occur, whereas cubic LLZO is disordered on its lithium sites and therefore sequential migration of lithium ions is possible.[13,14] Additionally, the lithium conduction pathway in cubic LLZO is 3 dimensional, whereas the conduction pathway in tetragonal LLZO is partially constrained along one axis [12].

The cubic phase of LLZO was originally stabilized by unintentional Al^{3+} doping from alumina crucibles during long and high temperature solid state synthesis [15,16]. Since then, a large number of other dopants have been explored to assess their effect on LLZO conductivity and stability [10,11,17]. A critical concentration of lithium vacancies around 0.6-0.8 Li per $Li_7La_3Zr_2O_{12}$ formula unit is typically required to stabilize the cubic structure with Al doping at room temperature [18,19]. This corresponds to 0.2-0.3 Al per $Li_7La_3Zr_2O_{12}$ [20], or approximately 2% of metal atoms. Staying below this level of aluminum content prevents conversion to cubic and has only a small impact on ionic conductivities [21]. It is also worth noting that the critical vacancy concentration varies for different dopants, with 0.4-0.5 being reported for Ta, for example [18]. Interestingly, although the current study is focused on undoped LLZO, we find that both the cubic and tetragonal phases are present in large areas of the phase stability diagram, such that the current study brings insight into decoupling the impacts of structure and composition described above.

Beyond structure and composition, the synthesis conditions have also been shown to have a large effect on total lithium conductivity, and a wide range of conductivities have been reported across a range of different synthesis methods. These syntheses include solid-state reactions, sol-gel, and various deposition techniques [10]. An in-situ neutron powder diffraction study using the solid-state reaction path has shown that an amorphous (melt) phase is present at temperatures as high as 950 °C [22]. By contrast, sol-gel samples have been synthesized as pure LLZO at 900 °C without any amorphous content [23,24], which is why sol-gel samples heated to 900 °C are selected as the primary focus in the current study. For undoped tetragonal LLZO, total conductivities vary over two orders of magnitude from the 5.67×10^{-5} S/cm reported by Zhao et al. [25] down to $\sim 2 \times 10^{-7}$ S/cm reported by Kokal et al. [26] and Toda et al. [27]. The sintering conditions used in the current study match those of Kokal et al. such that the value of $\sim 2 \times 10^{-7}$ S/cm is of highest relevance here. Total conductivity can be further separated into bulk and grain boundary contributions. Toda breaks down their total conductivity into 1.3×10^{-6} S/cm bulk conductivity and 2.2×10^{-7} S/cm grain boundary conductivity, [26] and Awaka et al. reports similar numbers with 1.63×10^{-6} S/cm bulk and 5.59×10^{-7} S/cm grain boundary conductivity [28]. Most authors do not report separate bulk and grain boundary conductivity however, making it difficult to analyze synthesis effects on bulk conductivity. Typically grain boundary resistance is minimized by sintering at high temperatures (1100-1200 °C) for a long time period (10-20 h) with either hot or cold pressing to approach a single crystal limit [29–32]. Under these conditions lithium volatilization can lead to the appearance of a problematic impurity phase, $\text{La}_2\text{Zr}_2\text{O}_7$, in the final product, and this phase increases the grain boundary resistance. Thus, 10% or more of excess lithium is routinely added to compensate [10,11].

Despite its importance, to date there has been no systematic study of the Li-La-Zr-O system. In fact, there remain very few systematic studies of pseudoternaries. High-throughput methods have proven extremely powerful in this regard. The entire Li-Ni-Mn-O pseudoternary system has been studied using high-throughput synthesis and powder X-ray diffraction. In that case, large solid solution regions were seen and their boundaries were systematically determined by using the lever rule [33–35]. The lever rule uses the phase compositions in co-existence regions to extrapolate to the boundaries of the co-existence. This means that 2-phase materials will extrapolate along a tie-line to single phase end members, and 3-phase materials will extrapolate to three 2-phase tie lines defining the borders of the coexistence region. By contrast, in the LLTO system, the lever rule systematically failed when it extrapolated to points where the LLTO phase was weaker and this demonstrated the stabilization caused by the secondary phases [8]. The lever rule therefore proves extremely insightful in understanding the phase stabilities at play in complex pseudoternary systems.

Herein, we studied the entire Li-La-Zr-O system via high throughput sol-gel synthesis at a variety of temperatures from 700 - 900°C. Figure 1a shows the compositions previously studied in the literature, while figure 1b shows the 184 compositions studied herein. Both structural (via X-ray diffraction) and electrolyte performance (via ionic conductivity) are reported and consequences of the developed phase stability (figure 1c) are discussed. In particular, this work helps explain a number of aspects related to garnet LLZO that remains unknown despite important research attention for a number of years. These include: explaining why pure cubic LLZO is difficult to synthesize without doping, why secondary $\text{La}_2\text{Zr}_2\text{O}_7$ is so devastating to ionic conductivities when present, and also demonstrates that some secondary phases may in fact improve ionic conductivities.

2. Experimental methods

We utilized a citrate sol-gel method to efficiently synthesize compositions covering the entire Li-La-Zr-O pseudoternary in a high-throughput manner, with 64 mg-scale samples being prepared at the same time as described in detail in refs. [24,36]. 350 μ L steel cups were arranged into an 8 \times 8 grid, and three separate plates were used to map out the entire pseudoternary system as demonstrated in ref. [8]. A total of 192 samples were therefore prepared at 120 distinct compositions (large black points in figure 1b), and 108 represent triplicates made to verify reproducibility (which is systematically found to be excellent as shown in refs. [8,24,36,37]). Additionally, another 8 \times 8 region was synthesized (indicated by the small densely packed black points in figure 1b) near the $\text{Li}_7\text{La}_3\text{Zr}_2\text{O}_{12}$ composition to improve our resolution around this critical phase.

Aqueous solutions of $\text{Li}(\text{NO}_3)$, $\text{La}(\text{NO}_3)_3$, and $\text{Zr}(\text{OH})_2(\text{OAc})_2$ were prepared and their concentrations were confirmed using inductively coupled plasma optical emission spectroscopy (ICP-OES). The solutions were pipetted in the desired ratio into the steel cups, and 4 M citric acid was added as a gelling agent. A molar ratio of 0.75:1 citric acid to metal ions was used, and the total solution volume was kept to 330 μ L. The gels were dried in air overnight at 110 $^\circ\text{C}$ to give a hard yellow foam showing no signs of retained moisture. The foam was then crushed to a powder and placed onto an alumina plate for calcination at 600 $^\circ\text{C}$ for 6 hours. The resulting white powders were crushed again and then pelleted at 750 MPa for 30 seconds to give cylindrical pellets 2 mm thick and 4.8 mm in diameter. The pellets were sintered in air on an alumina plate for 3 h at either 700, 800 or 900 $^\circ\text{C}$, with a heating and cooling rate of 5 $^\circ\text{C}/\text{min}$ in all cases.

The final composition of the resulting sintered pellets was determined using ICP-OES (for a few key compositions shown in figure 1d). The samples were also characterized using powder X-ray

diffraction (PXRD, all samples) and electrochemical impedance spectroscopy (EIS, all samples in the 8×8 region near $\text{Li}_7\text{La}_3\text{Zr}_2\text{O}_{12}$). ICP-OES measurements were performed by the Minerals Engineering Center at Dalhousie University. PXRD characterization was performed in high-throughput using a Panalytical Empyrean diffractometer equipped with a Mo anode (60 kV, 40 mA, 10 min scan, 4-30° scattering angles) and a GalaPIX area detector. The pellets were crushed into a fine powder via mortar and pestle prior to PXRD. All analysis/fitting was performed on the raw data, however, for ease of comparison with the literature all patterns presented in this article have been stripped of their $k_{\alpha,2}$ peaks and scattering angles have been converted to the Cu anode equivalents as is typical for the literature in this field.

The pellets were prepared for EIS characterization by first sanding the top and bottom flat using 800 grit sandpaper. Excess dust was removed by a short blast of compressed air, and the pellets were sputter coated with gold to ensure good electrical contact. The pellets were then placed into a custom 8×8 cell that applies pressure to all 64 pellets using spring mounted pistons. Impedance measurements were taken over a frequency range of 1 Hz to 1 MHz. The impedance spectra were fitted to an equivalent circuit containing one resistor/constant-phase (RQ) element each for bulk and grain boundary conduction as well as an additional Q element for Warburg diffusion, demonstrated in refs. [8,24] This high-throughput EIS system has been demonstrated to be precise and reproducible elsewhere [24,36]. For this set of samples, PXRD was performed after EIS.

3. Results and discussion

Figure 1A shows the Li-La-Zr-O pseudoternary with previously studied single phase materials indicated by colored dots. While the pseudobinaries have been well studied in the past, the only known pseudoternary material to date is LLZO itself [38–40]. Figure 1b overlays the 184 unique

compositions synthesized in this work as black dots. Careful PXRD analysis of these compositions led to the completed phase stability diagram for synthesis at 900 °C for 3 h shown in figure 1c. The basis for this phase stability will be discussed in detail below. Single phase points are shown as colored points, the red region indicates a solid-solution, the dashed red lines indicate 2-phase tie-lines bounding 3-phase regions and the dashed green lines are tie-lines in 2-phase regions. The large grey region extending from the Li-La pseudobinary is the region of extreme lithium loss where we find no stable phases under these synthesis conditions, as previously noted in ref. [8]. The grey region consistent with figure 1d showing the results from ICP-OES analysis of selected samples after sintering at 700, 800 or 900°C. In the high lithium region, lithium is lost until the samples reach the boundary of the grey region at 800 and 900 °C. Samples with less lithium show no lithium loss even at 900 °C. Although no lithium loss occurs at any composition at 700 °C, it is important to note that these samples show poor crystallinity as will be discussed further below. Given the concerns mentioned in the introduction with respect to inadvertent aluminum doping from the alumina substrate used during sintering, the ICP-OES included the search for aluminum which was systematically low (at. % of 0.7-1.0 % per total metals). The established threshold concentration of aluminum doping is approximately 2% per total metals, and so we conclude that the inadvertent doping in the current study has no impact on the structures and ionic conductivities, again similarly to our results in ref. [8].

Figure 2 shows PXRD patterns along 2 composition lines, along with reference patterns for the known phases. Figure 2b shows that single-phase Li-substituted $\text{La}_2\text{Zr}_2\text{O}_3$ is present well inside the pseudoternary system, and it also shows cross-over into a 3-phase region as we move to the right in the triangle, consistent with our phase stability. Similarly, Figure 2c shows cross-over between two 3-phase regions, again consistent with our phase stabilities. Although the exact

boundaries to these regions were determined using the lever rule as discussed further below, these PXRD patterns are useful guides to understand how the structures are evolving with composition.

There are therefore several notable features present in the diagram in Figure 1c, the most interesting being the large solid solution region extending from the La-Zr binary where we find significant Li solubility into the $\text{La}_2\text{Zr}_2\text{O}_7$ pyrochlore structure. $\text{La}_2\text{Zr}_2\text{O}_7$ is a well-known impurity phase that appears after excessive Li loss during LLZO synthesis, but literature reports have always assumed it to be the lithium free formal composition [22,41]. Despite this, it is well known that a wide variety of substitutions are possible in the pyrochlore family [42] and that Li inclusion in an already Er and Yb co-doped $\text{La}_2\text{Zr}_2\text{O}_7$ has also been reported [43]. It is therefore not completely unexpected that here, we find a Li-doped LZO solid solution with the Li-saturated composition indicated by the green point in Figure 1c. The XRD pattern of the sample nearest to this Li-saturated LZO was fit (figure 3c) using Rietveld refinement. We therefore added lithium into the LZO structure in order to match the composition predicted by the lever rule (discussed below). The structure of this Li-saturated LZO is shown in detail in the SI (table S1, figure S1 and discussion), but the key points are that lithium occupies both La sites (left partially vacant based on composition) and interstitial sites (0.25, 0.25, 0.25), and the material is charge balanced with oxygen vacancies (this is the only possibility given that La and Zr both have a single oxidation state). The fact that Li occupies two different sites can be used to explain why the solid solution line is not linear. As Li is added to $\text{La}_2\text{Zr}_2\text{O}_7$ (moving to the right along the red solid solution line in Fig. 1c), at first the La:Zr ratio remains constant implying that Li is taking interstitial sites, then as the line curves downward with more Li addition, the La:Zr ratio decreases indicating that at least some of the extra Li shares the La site. It is of note that the interstitial site (figure S1) yields minimum Li-O lengths of 2.09 Å (nearly identical to the 2.10 Å seen for LiCoO_2). This therefore

explains why the Li-saturated LZO material has only a very slightly smaller lattice parameter than $\text{La}_2\text{Zr}_2\text{O}_7$ (10.786 vs. 10.805 Å): the interstitial is large enough to harbor a Li without expanding the lattice, and the small amount of oxygen vacancies have a minimal impact on the lattice size. It is also noteworthy here that although the lithium content is high, there is no low energy path for lithium to migrate in this structure (the interstitials are all isolated), thus explaining why this material has a very low ionic conductivity (too low for us to measure with EIS, implying $< 10^{-8}$ S/cm as discussed below). Furthermore, the LLZO single phase point has been split to show the presence of both tetragonal and cubic LLZO. Although we find no single phase cubic LLZO, it is systematically present in the co-existence region on the low lithium side of LLZO. This will be discussed extensively below. Additionally, we note that ZrO_2 is present in both the monoclinic and tetragonal phases under these conditions, with a majority tetragonal ZrO_2 along the Zr-La binary and majority monoclinic ZrO_2 along the Li-Zr binary, consistent with refs. [38,44]. However, unlike cases seen in solid state syntheses, no ZrO_2 phase is present in samples made near the LLZO composition as demonstrated in Figure S3. This is likely the result of better mixing of precursors during the sol-gel process.

As mentioned above, the boundaries in the phase stability in figure 1c were determined using the lever rule. To do this, high quality Rietveld fits were performed on samples in both the single phase and the co-existence regions. Figure 3 shows single phase fits for all 7 phases present in the diagram. Figure 3g includes $\text{La}(\text{OH})_3$ that is often present as a hydration product in samples with high amounts of La_2O_3 . It was not found in samples with a significant amount of LLZO nor in any of the patterns that we used for the lever rule.

For all scans in figure 3, the fits are excellent and lattice parameters are typical for the materials shown. Figure 4a-c further shows that excellent fits are obtained for samples in the 3-phase regions.

All three scans in figure 4 are from samples with Li content lower than LLZO and were found to co-exist with cubic LLZO rather than tetragonal LLZO (fitting with a tetragonal reference pattern gave equal lattice parameters, as discussed further below). It should also be noted that an R_{wp} value will be considerably higher when the background is lower even for the exact same fit.[44] Here, Mo-radiation yields a very low background and this artificially inflates the R_{wp} values reported herein. For example, a background of 22-30 counts in Fig. 3a (this represents 0.8-1.2 % of the largest peak height) and this yields an R_{wp} of 20.6%. When we add 220 counts to the background in order to have a background that is the same fraction (11 %) of the largest peak height as in ref. [45] where Cu radiation is used, then the R_{wp} drops to 7.6 %. With Cu radiation XRD patterns, 10 % is typically considered to be an R_{wp} for a quality fit. With our Mo radiation patterns here, an R_{wp} of 27 % becomes 8 % when the background is adjusted to be 11% of the largest peak as described above. Thus, we consider any R_{wp} of 27 % or below to represent quality fits. As shown in the SI, all fits performed herein have R_{wp} values in this range, with the vast majority being below 15 %, indicating high quality of fits. All lattice parameters and R_{wp} values extracted in this study are presented in tables S2-S9.

Using the phase compositions obtained from the resulting fits, the lever rule was systematically applied in figure 4d. The small colored points correspond to extrapolation points obtained from the larger points of the same color (which represent single phase points). For example, we can see that in the upper three-phase region containing La_2O_3 , a Li-substituted $\text{La}_2\text{Zr}_2\text{O}_7$, and LLZO, the large single-phase points are each opposite a line of identically colored points generated by applying the lever rule. The position of the two single phase points in the red solid solution were adjusted until all extrapolated points were self-consistent. Note: when $\text{La}_2\text{Zr}_2\text{O}_7$ at its formal composition was used as the reference point, many of the extrapolated points fell well outside of

the ternary diagram, indicating that the chosen reference point is at the incorrect composition. The selected positions, however, yield proper extrapolation to the expected binary tie-lines between the other single phase points (e.g. the LLZO and the La_2O_3 corners) to correctly define 3-phase coexistence regions. This clearly demonstrates that the Li-substituted $\text{La}_2\text{Zr}_2\text{O}_7$ solid solution region exists and extends well into the pseudoternary region. The boundaries of the two 3-phase regions shown in figure 4d do not share a boundary and they therefore leave a small region in between. This region in between is difficult to identify given its small composition range, but we tentatively assign this to a 2-phase region tying to LLZO. However, quenching studies should be performed should this prove important to confirm, given that trace amounts of La_2O_3 were found in the slow cooled samples in this small 2-phase region. The two other 3-phase regions in figure 1c are found simply from the position of the single phase materials bounding those regions as they appear in the PXRD analysis, it was the identification of the position of the Li-substituted $\text{La}_2\text{Zr}_2\text{O}_7$ phase that required the use of the lever rule. The boundary to the Li-substituted LZO phase was simply obtained by connecting the dots from the lever rule. Our data shows no evidence that this region has a significant width.

The systematic PXRD study of the Li-La-Zr-O diagram yields a few points of interest that require further attention. The first is that garnet LLZO patterns fitting best as either cubic or tetragonal are both obtained. Figure 5 shows resulting contour plots obtained for the LLZO lattice parameters when fit as tetragonal (note: these are results from multi-phase fits when appropriate such that there are no distortions due to secondary phases). The results clearly show that on the low lithium content side of LLZO, the structure is systematically cubic, while on the high lithium content side it is tetragonal. This is also illustrated in a traditional plot in Figure S2. Furthermore, the transition between the two structures is consistent with the boundaries of the extreme lithium loss region

shown in grey in figure 1c. As such, we conclude that the LLZO region is in fact a small solid solution with the lithium deficient part being very restrained in composition (i.e. LLZO does not tolerate many lithium vacancies without doping). We speculate that the charge compensation accounting for the lithium deficiency comes from a small number of oxygen vacancies, but this requires further investigation. Combining the fact that it is such a small solid solution with the fact that lithium loss is extreme makes single-phase cubic-LLZO extremely difficult to synthesize without doping. Furthermore, given that the $\text{La}_2\text{Zr}_2\text{O}_7$ region extends far into the pseudoternary, this phase is present in far higher amounts than expected when lithium loss occurs (i.e. a small amount of lithium loss will yield more of this secondary phase than expected due to the solid solution being so close). These results therefore help explain many of the challenges encountered to date in trying to stabilize undoped cubic LLZO.

Up to now, we have discussed the results after synthesis at 900°C primarily because these samples show the best crystallinity and thereby were the easiest to analyze. Overall, the results at 700 and 800 °C are consistent with the phase stabilities shown for 900 °C in the sense that no other phase was seen. However, the peak widths are broadened significantly and there is some indication of amorphous content present, particularly at 700 °C (see fig. S4). Figure 6 clearly shows that lower crystallinity is systematically observed at lower temperatures, but despite this we can still see that Li-substituted $\text{La}_2\text{Zr}_2\text{O}_7$ solid solution extends well into the pseudoternary even after heating at 700 °C. It is also interesting to note the extent to which the presence of lithium yields higher crystallinity than the lithium-free composition, especially at the lower temperatures. That is, lithium provides accelerated crystal growth in the $\text{La}_2\text{Zr}_2\text{O}_7$ phase at all temperatures, with the effect being particularly dramatic at 700 °C.

As a final point on the PXRD patterns, figure 7 shows that a phase not discussed above appears at a composition in the region of extreme lithium loss when the samples are slow cooled at 5 °C/min in air. This phase appears irregularly in the lithium loss region except for on the Li-La binary where this phase was never observed. However, this phase is not present in samples quenched by placing on a steel slab in air (roughly 1 min to get to <100 °C) as shown in figure 7b. We therefore conclude that this phase is forming during slower cooling. This phase has been seen once previously in a citrate-nitrate auto-combustion synthesis of LLZO [46], and identified as being isostructural with $\text{Li}_8\text{FeSm}_{22}\text{O}_{38}$ [47]. Given similar ionic radii and the position in the phase diagram, we performed fits assuming $\text{Li}_8\text{ZrLa}_{22}\text{O}_{38}$ and obtain high quality fits (fitting results in Table S9). Figure 7b shows that the reference pattern for $\text{Li}_8\text{ZrLa}_{22}\text{O}_{38}$ generated herein matches well with all peaks for this phase. Further study with extreme slow cooling, holds during cooling, or a modified atmosphere may be required to isolate this phase. This type of transformation during cooling is not new to battery materials research and has been seen in lithium ion cathodes (e.g. ref. [33]). It occurs when the phase(s) stabilized at high-temperature are not the stable phase(s) at some intermediate temperature during cooling, such that slow cooling results in partial transformation. It is critical that materials researchers be aware of such cases, especially given how difficult it is to control cooling rates in large batches used in large-scale syntheses.

Finally, the interest of LLZO as a solid electrolyte is important and we aim here to determine the impact of the phase stability of the pseudoternary Li-La-Zr-O system on ionic conductivities. Figure 8a,b show representative electrochemical impedance spectra for two representative samples. The fits were obtained using the two RQ element circuit discussed in the experimental section and in our other publications [8,24]. We obtain two contributions to the EIS spectra by fitting in this manner. The attribution of the two semicircles to the grain boundary and bulk

contributions was done in a way that was consistent with previous literature for tetragonal LLZO obtained after sintering at a similar temperature (ref. [26]). In this manner, we obtain a grain boundary conductivity of 3.1×10^{-7} S/cm (compared to 5.59×10^{-7} S/cm from ref. [26]) while in both cases the bulk conductivities are at least an order of magnitude higher such that mistaking the bulk and grain boundary contributions is impossible. It is therefore far easier to attribute the bulk and grain boundary contributions here than is often the case for doped LLZO.

Figure 8c shows the resulting bulk ionic conductivities. As shown in ref. [21], aluminum doping seen in our samples (0.07 – 0.10 Al per formula unit) gives a small increase in conductivity compared to undoped LLZO and yields results near 1.5×10^{-5} S/cm, in good agreement with our results here for bulk conductivity. Nonetheless, ref. [21] also shows these aluminum contents are well below the level needed to get the large boost in conductivity seen in the Al-doped cubic LLZO. Interestingly, the bulk conductivities are nearly constant across the entire region, with only a small increase in the low-lithium region where the cubic LLZO phase is present. The highest content t-LLZO is 100% based on XRD analysis and it had a bulk conductivity of 1.17×10^{-5} S/cm. The highest content c-LLZO reported here is 87% with 9.8% Li_2ZrO_3 and 3.0 % LZO and its bulk conductivity is 1.83×10^{-5} S/cm. The challenge in trying to obtain higher c-LLZO content is related to the fact that this phase is in proximity to the region of extreme lithium loss such that lithium gradients are undoubtedly created within particles and the surface is either so lithium deficient that it has co-existence with LZO, or the core remains non-lithium deficient and still tetragonal. We conclude that for the heating/cooling protocol described here, 87 % represents an optimum c-LLZO content. Nonetheless, we believe that the secondary phases do not affect the bulk conductivity of the samples significantly. This becomes evident when examining the t-LLZO containing samples in the zoomed-in region. For example, the sample made at the composition

(Li,La) = (0.643,0.245) containing 83 % t-LLZO along with 11 % La_2O_3 and 6 % $\text{Li}_8\text{ZrLa}_{22}\text{O}_{38}$ had a bulk conductivity of 1.39×10^{-5} S/cm, in excellent agreement with the value of 1.17×10^{-5} S/cm obtained for pure t-LLZO. This is consistent with the fact that bulk conductivity values are weakly impacted by secondary phases as long as the most conductive phase is above the percolation threshold as is the case in all our samples in the zoomed in region where we perform EIS measurements. Given that the bulk conductivity remains nearly constant with varying c-LLZO content, we conclude that the c-LLZO made here does not have an appreciably higher bulk conductivity than the t-LLZO. Thus, the improvement in the cubic phase bulk conductivity is less than a factor of 2, such that we propose that the dramatic improvement in ionic conductivities in the cubic phase vs tetragonal phases reported previously in the literature for doped samples (2 orders of magnitude as discussed in the introduction) certainly require the change in structure, but also relies heavily on the impact of the dopants themselves and the Li vacancies they induce. It is also worth noting that this result is in contrast to reports that show undoped LLZO has a large jump in conductivity when heated across the tetragonal to cubic transition near 625 °C [48], implying that the cubic phase synthesized here and stable at room temperature is in fact slightly different from that obtained by heating the tetragonal phase to high temperature. Figure 8d shows the map for the grain boundary conductivities. It is interesting to note that the grain boundary conductivities are too low to measure in the region where cubic LLZO co-exists (i.e. lithium content below that of LLZO). This can be attributed to the presence of the Li-substituted $\text{La}_2\text{Zr}_2\text{O}_7$ phase and clearly demonstrates that this region must be avoided at all cost. This highest conductivity obtained herein is 3.8×10^{-7} S/cm, slightly higher than the results from Tokal *et al.* under similar conditions as discussed in the introduction (2×10^{-7} S/cm) showing a slight benefit to optimizing composition in this system. Although very different in morphology, the conductivities obtained here are also

comparable to those obtained by thin film techniques for undoped LLZO (10^{-8} to 10^{-6} S/cm) [10], indicating that our high-throughput results are consistent with thin film syntheses that typically use a sintering step that does not exceed our sintering temperature of 900 °C. Furthermore, this particular sample showing highest grain boundary conductivity in our study had the following phase composition according to PXRD of 7.4 wt. % La_2O_3 , 2.5 wt. % $\text{Li}_8\text{ZrLa}_{22}\text{O}_{38}$, and 90.1 wt. % LLZO. Samples lower in the phase stability diagram, some of which were pure phase tetragonal LLZO, had lower grain boundary conductivities. As was the case in the Li-La-Ti-O [8], we again find here that it is not the purest phase samples that give the highest grain boundary conductivities, but instead secondary phases are beneficial in lowering grain boundary resistances.

4. Conclusions

We successfully applied high-throughput methods to synthesize and characterize over 700 samples in the Li-La-Zr-O pseudoternary system. The resulting phase stability diagram for samples synthesized at 900 °C showed two important results of note to the solid electrolyte research community. A solid solution region was found where Li is highly soluble in the $\text{La}_2\text{Zr}_2\text{O}_7$ pyrochlore structure, occupying both La sites and interstitial sites that are large enough to accommodate lithium without significant expansion of the lattice. The crystal growth in this phase was found to be greatly accelerated by the presence of lithium. Additionally, we find that the $\text{Li}_7\text{La}_3\text{Zr}_2\text{O}_{12}$ garnet phase of highest interest to battery research was found to be a very restrained solid solution where the lithium deficient region yields a cubic phase and the lithium excess region yields a tetragonal phase.

The resulting analysis of impedance spectra demonstrated that the ionic conductivity of the cubic phase is marginally higher than that of the tetragonal phase, such that we conclude that orders of

magnitude improvements seen in other reports require both the conversion to cubic and the change in composition (presence of dopant and Li vacancy) rather than being solely attributable to the benefits of the cubic structure itself. Our results also show that the Li-substituted pyrochlore phase is highly detrimental to grain boundary conductivity and must be avoided. This is particularly noteworthy because the high lithium content in this phase means that it appears in much greater proportions than would be expected if it only existed at the formal $\text{La}_2\text{Zr}_2\text{O}_7$ composition. This study provides useful insights into previously unexplained results in this system of high interest and will enable further study including a systematic high-throughput study of the impacts of dopants into the LLZO structure.

Acknowledgements:

This work is dedicated to the memory of professor Michael Buschmann, who – along with his wife Caroline – provided EA a home away from home during undergraduate studies, and gave valuable advice during graduate research and the writing of this article.

This work was funded by a New Frontiers Research Fund, by the Natural Sciences and Engineering Research Council of Canada under the auspices of a Discovery grant, and by the FRQNT.

References

- [1] M. Li, J. Lu, Z. Chen, K. Amine, 30 Years of Lithium-Ion Batteries, *Adv. Mater.* 30 (2018) 1800561. <https://doi.org/10.1002/adma.201800561>.
- [2] G.E. Blomgren, The Development and Future of Lithium Ion Batteries, *J. Electrochem. Soc.* 164 (2017) A5019–A5025. <https://doi.org/10.1149/2.0251701jes>.
- [3] R. Wang, W. Cui, F. Chu, F. Wu, Lithium metal anodes: Present and future, *J. Energy Chem.* 48 (2020) 145–159. <https://doi.org/10.1016/j.jechem.2019.12.024>.
- [4] J. Kalhoff, G.G. Eshetu, D. Bresser, S. Passerini, Safer Electrolytes for Lithium-Ion Batteries: State of the Art and Perspectives, *ChemSusChem.* 8 (2015) 2154–2175. <https://doi.org/10.1002/cssc.201500284>.
- [5] D. Lin, Y. Liu, Y. Cui, Reviving the lithium metal anode for high-energy batteries, *Nat. Nanotechnol.* 12 (2017) 194–206. <https://doi.org/10.1038/nnano.2017.16>.
- [6] Y. Ren, K. Chen, R. Chen, T. Liu, Y. Zhang, C.-W. Nan, Oxide Electrolytes for Lithium Batteries, *J. Am. Ceram. Soc.* 98 (2015) 3603–3623. <https://doi.org/10.1111/jace.13844>.

- [7] T. Ye, L. Li, Y. Zhang, Recent Progress in Solid Electrolytes for Energy Storage Devices, *Adv. Funct. Mater.* 30 (2020) 2000077. <https://doi.org/10.1002/adfm.202000077>.
- [8] A. Jonderian, M. Ting, E. McCalla, Metastability in Li–La–Ti–O Perovskite Materials and Its Impact on Ionic Conductivity, *Chem. Mater.* 33 (2021) 4792–4804. <https://doi.org/10.1021/acs.chemmater.1c01490>.
- [9] S. Qin, X. Zhu, Y. Jiang, M. Ling, Z. Hu, J. Zhu, Growth of self-textured Ga³⁺-substituted Li₇La₃Zr₂O₁₂ ceramics by solid state reaction and their significant enhancement in ionic conductivity, *Appl. Phys. Lett.* 112 (2018) 113901. <https://doi.org/10.1063/1.5019179>.
- [10] A.J. Samson, K. Hofstetter, S. Bag, V. Thangadurai, A bird's-eye view of Li-stuffed garnet-type Li₇La₃Zr₂O₁₂ ceramic electrolytes for advanced all-solid-state Li batteries, *Energy Environ. Sci.* 12 (2019) 2957–2975. <https://doi.org/10.1039/C9EE01548E>.
- [11] Q. Liu, Z. Geng, C. Han, Y. Fu, S. Li, Y. He, F. Kang, B. Li, Challenges and perspectives of garnet solid electrolytes for all solid-state lithium batteries, *J. Power Sources.* 389 (2018) 120–134. <https://doi.org/10.1016/j.jpowsour.2018.04.019>.
- [12] F. Chen, J. Li, Z. Huang, Y. Yang, Q. Shen, L. Zhang, Origin of the Phase Transition in Lithium Garnets, *J. Phys. Chem. C.* 122 (2018) 1963–1972. <https://doi.org/10.1021/acs.jpcc.7b10911>.
- [13] R. Jalem, Y. Yamamoto, H. Shiiba, M. Nakayama, H. Munakata, T. Kasuga, K. Kanamura, Concerted Migration Mechanism in the Li Ion Dynamics of Garnet-Type Li₇La₃Zr₂O₁₂, *Chem. Mater.* 25 (2013) 425–430. <https://doi.org/10.1021/cm303542x>.
- [14] K. Meier, T. Laino, A. Curioni, Solid-State Electrolytes: Revealing the Mechanisms of Li-Ion Conduction in Tetragonal and Cubic LLZO by First-Principles Calculations, *J. Phys. Chem. C.* 118 (2014) 6668–6679. <https://doi.org/10.1021/jp5002463>.
- [15] R. Murugan, V. Thangadurai, W. Weppner, Fast Lithium Ion Conduction in Garnet-Type Li₇La₃Zr₂O₁₂, *Angew. Chem. Int. Ed.* 46 (2007) 7778–7781. <https://doi.org/10.1002/anie.200701144>.
- [16] C.A. Geiger, E. Alekseev, B. Lazic, M. Fisch, T. Armbruster, R. Langner, M. Fechtelkord, N. Kim, T. Pettke, W. Weppner, Crystal Chemistry and Stability of “Li₇La₃Zr₂O₁₂” Garnet: A Fast Lithium-Ion Conductor, *Inorg. Chem.* 50 (2011) 1089–1097. <https://doi.org/10.1021/ic101914e>.
- [17] S. Cao, S. Song, X. Xiang, Q. Hu, C. Zhang, Z. Xia, Y. Xu, W. Zha, J. Li, P.M. Gonzalez, Y.-H. Han, F. Chen, Modeling, Preparation, and Elemental Doping of Li₇La₃Zr₂O₁₂ Garnet-Type Solid Electrolytes: A Review, *J. Korean Ceram. Soc.* 56 (2019) 111–129. <https://doi.org/10.4191/kcers.2019.56.2.01>.
- [18] T. Thompson, J. Wolfenstine, J. L. Allen, M. Johannes, A. Huq, I. N. David, J. Sakamoto, Tetragonal vs. cubic phase stability in Al – free Ta doped Li₇La₃Zr₂O₁₂ (LLZO), *J. Mater. Chem. A.* 2 (2014) 13431–13436. <https://doi.org/10.1039/C4TA02099E>.
- [19] N. Bernstein, M.D. Johannes, K. Hoang, Origin of the Structural Phase Transition in Li₇La₃Zr₂O₁₂, *Phys. Rev. Lett.* 109 (2012) 205702. <https://doi.org/10.1103/PhysRevLett.109.205702>.
- [20] E. Rangasamy, J. Wolfenstine, J. Sakamoto, The role of Al and Li concentration on the formation of cubic garnet solid electrolyte of nominal composition Li₇La₃Zr₂O₁₂, *Solid State Ion.* 206 (2012) 28–32. <https://doi.org/10.1016/j.ssi.2011.10.022>.
- [21] L. Zhuang, X. Huang, Y. Lu, J. Tang, Y. Zhou, X. Ao, Y. Yang, B. Tian, Phase transformation and grain-boundary segregation in Al-Doped Li₇La₃Zr₂O₁₂ ceramics, *Ceram. Int.* 47 (2021) 22768–22775. <https://doi.org/10.1016/j.ceramint.2021.04.295>.

- [22] R.P. Rao, W. Gu, N. Sharma, V.K. Peterson, M. Avdeev, S. Adams, In Situ Neutron Diffraction Monitoring of $\text{Li}_7\text{La}_3\text{Zr}_2\text{O}_{12}$ Formation: Toward a Rational Synthesis of Garnet Solid Electrolytes., *Chem. Mater.* 27 (2015) 2903–2910. <https://doi.org/10.1021/acs.chemmater.5b00149>.
- [23] J. Li, Z. Liu, W. Ma, H. Dong, K. Zhang, R. Wang, Low-temperature synthesis of cubic phase $\text{Li}_7\text{La}_3\text{Zr}_2\text{O}_{12}$ via sol-gel and ball milling induced phase transition, *J. Power Sources.* 412 (2019) 189–196. <https://doi.org/10.1016/j.jpowsour.2018.11.040>.
- [24] E. McCalla, M. Parmaklis, S. Rehman, E. Anderson, S. Jia, A. Hebert, K. Potts, A. Jonderian, T. Adhikari, M. Adamič, Combinatorial methods in advanced battery materials design, *Can. J. Chem.* 100 (2022) 132–143. <https://doi.org/10.1139/cjc-2021-0111>.
- [25] P. Zhao, Y. Wen, J. Cheng, G. Cao, Z. Jin, H. Ming, Y. Xu, X. Zhu, A novel method for preparation of high dense tetragonal $\text{Li}_7\text{La}_3\text{Zr}_2\text{O}_{12}$, *J. Power Sources.* 344 (2017) 56–61. <https://doi.org/10.1016/j.jpowsour.2017.01.088>.
- [26] I. Kokal, M. Somer, P.H.L. Notten, H.T. Hintzen, Sol-gel synthesis and lithium ion conductivity of $\text{Li}_7\text{La}_3\text{Zr}_2\text{O}_{12}$ with garnet-related type structure, *Solid State Ion.* 185 (2011) 42–46. <https://doi.org/10.1016/j.ssi.2011.01.002>.
- [27] S. Toda, K. Ishiguro, Y. Shimonishi, A. Hirano, Y. Takeda, O. Yamamoto, N. Imanishi, Low temperature cubic garnet-type CO_2 -doped $\text{Li}_7\text{La}_3\text{Zr}_2\text{O}_{12}$, *Solid State Ion.* 233 (2013) 102–106. <https://doi.org/10.1016/j.ssi.2012.12.007>.
- [28] J. Awaka, N. Kijima, H. Hayakawa, J. Akimoto, Synthesis and structure analysis of tetragonal $\text{Li}_7\text{La}_3\text{Zr}_2\text{O}_{12}$ with the garnet-related type structure, *J. Solid State Chem.* 182 (2009) 2046–2052. <https://doi.org/10.1016/j.jssc.2009.05.020>.
- [29] E. Rangasamy, J. Wolfenstine, J. Allen, J. Sakamoto, The effect of 24c-site (A) cation substitution on the tetragonal-cubic phase transition in $\text{Li}_{7-x}\text{La}_3-x\text{AxZr}_2\text{O}_{12}$ garnet-based ceramic electrolyte, *J. Power Sources.* 230 (2013) 261–266. <https://doi.org/10.1016/j.jpowsour.2012.12.076>.
- [30] H. Buschmann, J. Dölle, S. Berendts, A. Kuhn, P. Bottke, M. Wilkening, P. Heitjans, A. Senyshyn, H. Ehrenberg, A. Lotnyk, V. Duppel, L. Kienle, J. Janek, Structure and dynamics of the fast lithium ion conductor “ $\text{Li}_7\text{La}_3\text{Zr}_2\text{O}_{12}$,” *Phys. Chem. Chem. Phys.* 13 (2011) 19378. <https://doi.org/10.1039/c1cp22108f>.
- [31] J. Wolfenstine, E. Rangasamy, J.L. Allen, J. Sakamoto, High conductivity of dense tetragonal $\text{Li}_7\text{La}_3\text{Zr}_2\text{O}_{12}$, *J. Power Sources.* 208 (2012) 193–196. <https://doi.org/10.1016/j.jpowsour.2012.02.031>.
- [32] R. Inada, K. Kusakabe, T. Tanaka, S. Kudo, Y. Sakurai, Synthesis and properties of Al-free $\text{Li}_{7-x}\text{La}_3\text{Zr}_2-x\text{TaxO}_{12}$ garnet related oxides, *Solid State Ion.* 262 (2014) 568–572. <https://doi.org/10.1016/j.ssi.2013.09.008>.
- [33] E. McCalla, A.W. Rowe, R. Shunmugasundaram, J.R. Dahn, Structural Study of the Li–Mn–Ni Oxide Pseudoternary System of Interest for Positive Electrodes of Li-Ion Batteries, *Chem. Mater.* 25 (2013) 989–999. <https://doi.org/10.1021/cm4001619>.
- [34] E. McCalla, C.M. Lowartz, C.R. Brown, J.R. Dahn, Formation of Layered–Layered Composites in the Li–Co–Mn Oxide Pseudoternary System during Slow Cooling, *Chem. Mater.* 25 (2013) 912–918. <https://doi.org/10.1021/cm304002b>.
- [35] C.R. Brown, E. McCalla, J.R. Dahn, Analysis of the cubic spinel region of the Li–Co–Mn oxide pseudo-ternary system, *Solid State Ion.* 253 (2013) 234–238. <https://doi.org/10.1016/j.ssi.2013.09.051>.

- [36] A. Jonderian, E. Anderson, R. Peng, P. Xu, S. Jia, V. Cozea, E. McCalla, Suite of High-Throughput Experiments for Screening Solid Electrolytes for Li Batteries, *J. Electrochem. Soc.* 169 (2022) 050504. <https://doi.org/10.1149/1945-7111/ac6a15>.
- [37] S. Jia, J. Counsell, M. Adamič, A. Jonderian, E. McCalla, High-throughput design of Na–Fe–Mn–O cathodes for Na-ion batteries, *J. Mater. Chem. A*. 10 (2022) 251–265. <https://doi.org/10.1039/D1TA07940A>.
- [38] G.P. Wyers, E.H.P. Cordfunke, Phase relations in the system Li₂O–ZrO₂, *J. Nucl. Mater.* 168 (1989) 24–30. [https://doi.org/10.1016/0022-3115\(89\)90560-6](https://doi.org/10.1016/0022-3115(89)90560-6).
- [39] F. Abbattista, M. Vallino, Remarks on the La₂O₃–Li₂O binary system between 750° and 1000°C, *Ceram. Int.* 9 (1983) 35–38. [https://doi.org/10.1016/0272-8842\(83\)90019-6](https://doi.org/10.1016/0272-8842(83)90019-6).
- [40] O. Fabrichnaya, S. Lakiza, Ch. Wang, M. Zinkevich, F. Aldinger, Assessment of thermodynamic functions in the ZrO₂–La₂O₃–Al₂O₃ system, *J. Alloys Compd.* 453 (2008) 271–281. <https://doi.org/10.1016/j.jallcom.2006.11.102>.
- [41] C. Deviannapoorani, S. Ramakumar, N. Janani, R. Murugan, Synthesis of lithium garnets from La₂Zr₂O₇ pyrochlore, *Solid State Ion.* 283 (2015) 123–130. <https://doi.org/10.1016/j.ssi.2015.10.006>.
- [42] P.S. Maram, S.V. Ushakov, R.J.K. Weber, C.J. Benmore, A. Navrotsky, Probing disorder in pyrochlore oxides using in situ synchrotron diffraction from levitated solids—A thermodynamic perspective, *Sci. Rep.* 8 (2018) 10658. <https://doi.org/10.1038/s41598-018-28877-x>.
- [43] S.K. Gupta, M. Abdou, J.P. Zuniga, P.S. Ghosh, Y. Mao, Li⁺ co-doping induced phase transition as an efficient strategy to enhance upconversion of La₂Zr₂O₇:Er, Yb nanoparticles, *J. Lumin.* 224 (2020) 117312. <https://doi.org/10.1016/j.jlumin.2020.117312>.
- [44] Toby, B. (2006). R factors in Rietveld analysis: How good is good enough? *Powder Diffraction*, 21(1), 67-70. doi:10.1154/1.2179804
- [45] E. Hanc, W. Zając, J. Molenda, Synthesis procedure and effect of Nd, Ca and Nb doping on structure and electrical conductivity of Li₇La₃Zr₂O₁₂ garnets, *Solid State Ion.* 262 (2014) 617–621. <https://doi.org/10.1016/j.ssi.2013.11.033>.
- [46] R.L. Sacci, R.D. McAuliffe, T.F. Malkowski, N. Kidder, X.C. Chen, A. Huq, M. Kirkham, B.L. Armstrong, L.L. Daemen, G.M. Veith, La₂Zr₂O₇ Nanoparticle-Mediated Synthesis of Porous Al-Doped Li₇La₃Zr₂O₁₂ Garnet, *Inorg. Chem.* 60 (2021) 10012–10021. <https://doi.org/10.1021/acs.inorgchem.1c01300>.
- [47] A.M. Vorotynov, G.A. Petrakovskii, D.A. Velikanov, L.V. Udod, M.S. Molokeyev, Synthesis, crystal structure, and magnetic properties of the Li₈FeSm₂Zr₃O₃₈ single crystal, *Phys. Solid State.* 54 (2012) 1796–1799. <https://doi.org/10.1134/S1063783412090302>.
- [48] Y. Wang, W. Lai, Phase transition in lithium garnet oxide ionic conductors Li₇La₃Zr₂O₁₂: The role of Ta substitution and H₂O/CO₂ exposure, *J. Power Sources.* 275 (2015) 612–620. <https://doi.org/10.1016/j.jpowsour.2014.11.062>.

Figures:

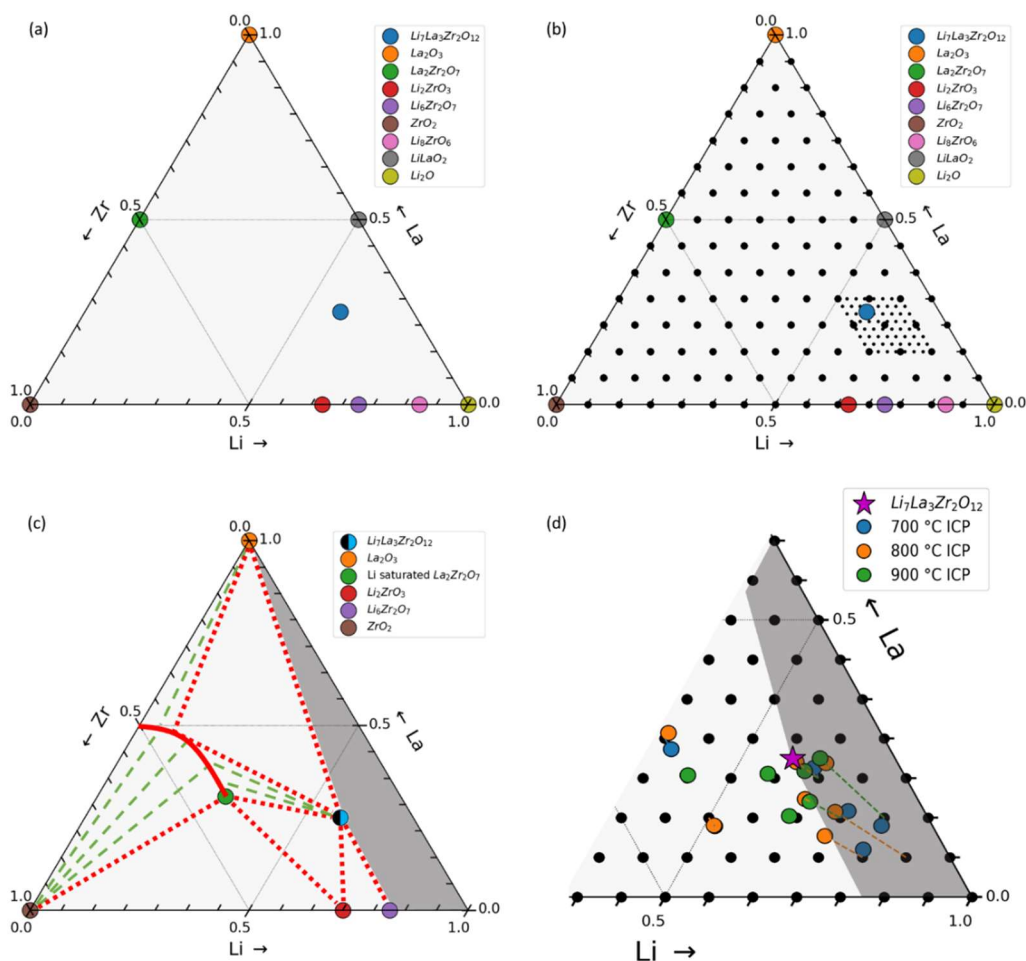


Figure 1: (a) The Li-La-Zr-O pseudoternary phase stability diagram with previously studied compositions only. (b) The phase stability diagram with black dots representing compositions synthesized for this study. (c) Resulting phase stability diagram for synthesis at 900 °C: single phase points are represented by colored dots, a solid-solution region is represented in solid red, tie-lines bounding 3-phase regions are red dashed lines, and tie lines in two-phase regions are represented by dashed green lines. The region of extreme lithium loss is shown in grey. $\text{Li}_7\text{La}_3\text{Zr}_2\text{O}_{12}$ (LLZO) is shown with a split blue/black point to indicate the very small solid solution region discussed in the text. (d) ICP-OES analysis of select compositions: the dashed line connect the dispensed compositions in black to the measured composition after synthesis.

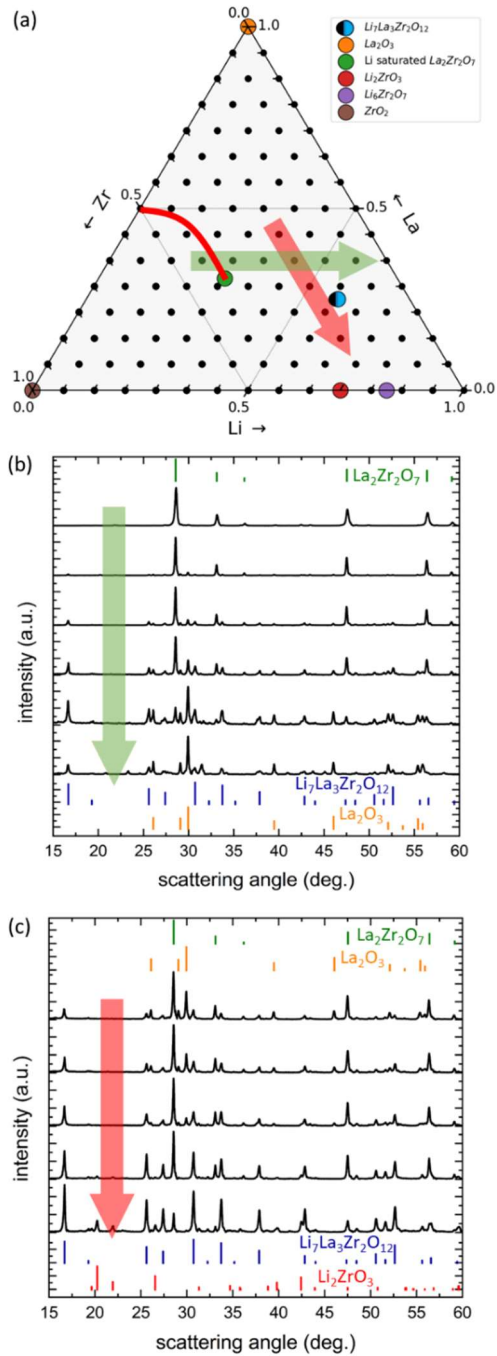


Figure 2: Pseudoternary diagram obtained after heating to 900 °C (a) with two composition lines indicated with their resulting PXRD patterns in (b) and (c). Relevant reference patterns are also shown in panels b and c. All phase identifications are consistent with the phase stabilities in Figure 1c.

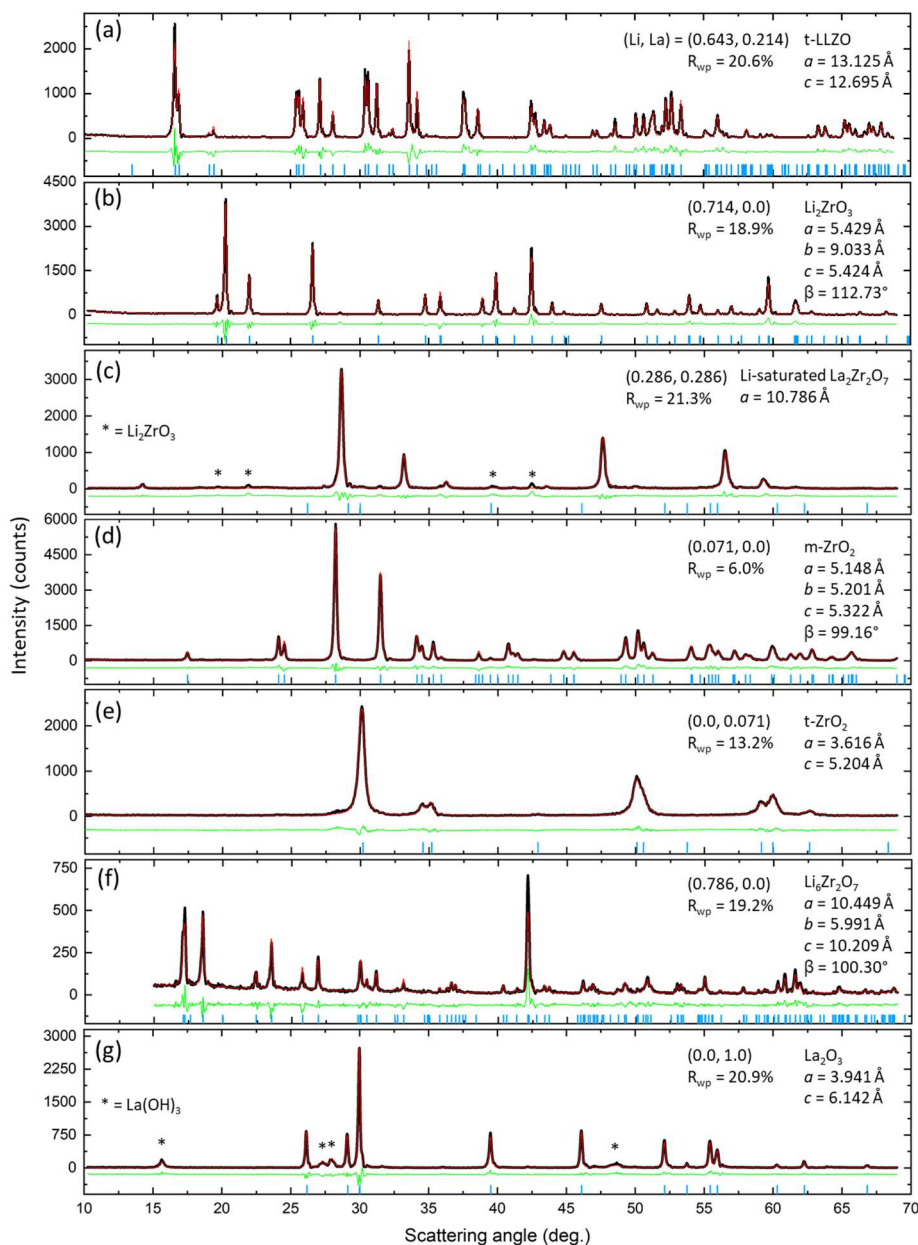


Figure 3: Rietveld refinements of single-phase samples obtained after heating to 900 °C: (a) tetragonal $\text{Li}_7\text{La}_3\text{Zr}_2\text{O}_{12}$ (ICSD #246817), (b) Li_2ZrO_3 (ICSD #94896), (c) Li-saturated $\text{La}_2\text{Zr}_2\text{O}_7$ (ICSD #153222, adapted as discussed in SI), (d) monoclinic ZrO_2 (ICSD #80048), (e) tetragonal ZrO_2 (ICSD #248448), (f) $\text{Li}_6\text{Zr}_2\text{O}_7$ (ICSD #73835), and (g) La_2O_3 (ICSD #28555). Note: La(OH)_3 (ICSD #167480) was also fit prior to using the lever rule. The notation (Li,La) is used for molar fraction of Li and La, while Zr is simply $1 - \text{Li} - \text{La}$.

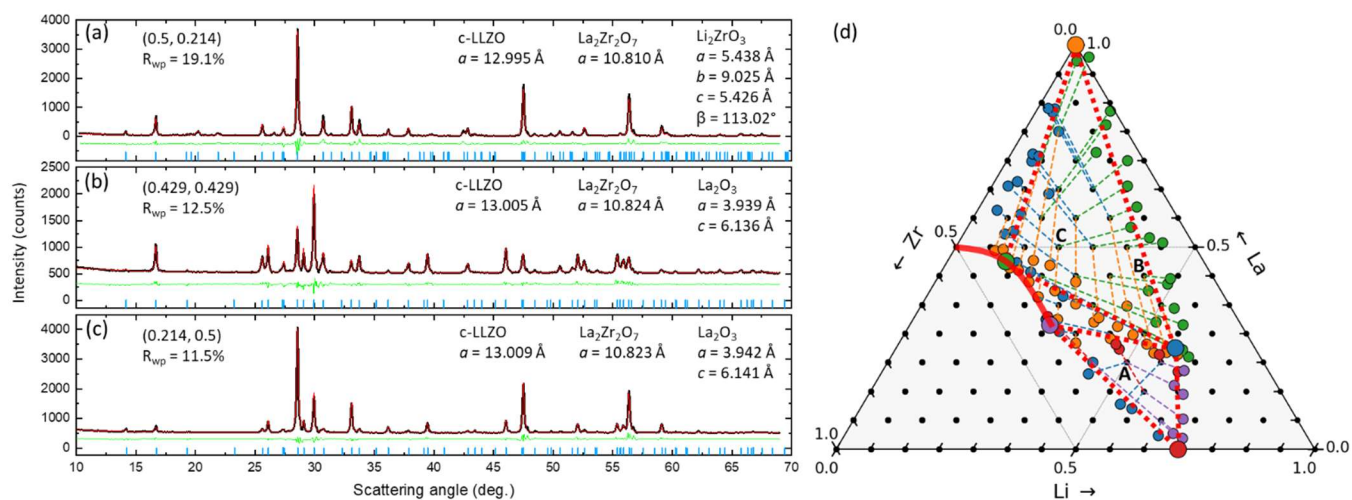


Figure 4: (a-c) Rietveld refinements of 3-phase samples at the compositions indicated in the pseudoternary after synthesis at 900 °C (d). The pseudoternary also shows the results of applying the lever rule to the phase compositions obtained in the 3-phase regions involving LLZO.

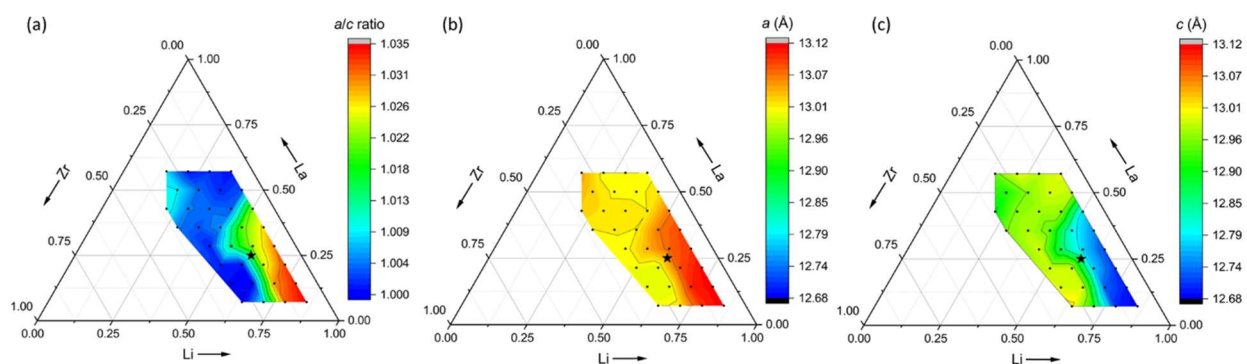


Figure 5: (a) Heat map of the lattice parameter ratio a/c for the $\text{Li}_7\text{La}_3\text{Zr}_2\text{O}_{12}$ phases all fit as tetragonal. The heat maps for the a lattice parameter is shown in (b) while the c parameters are shown in (c). All samples were synthesized at 900 °C.

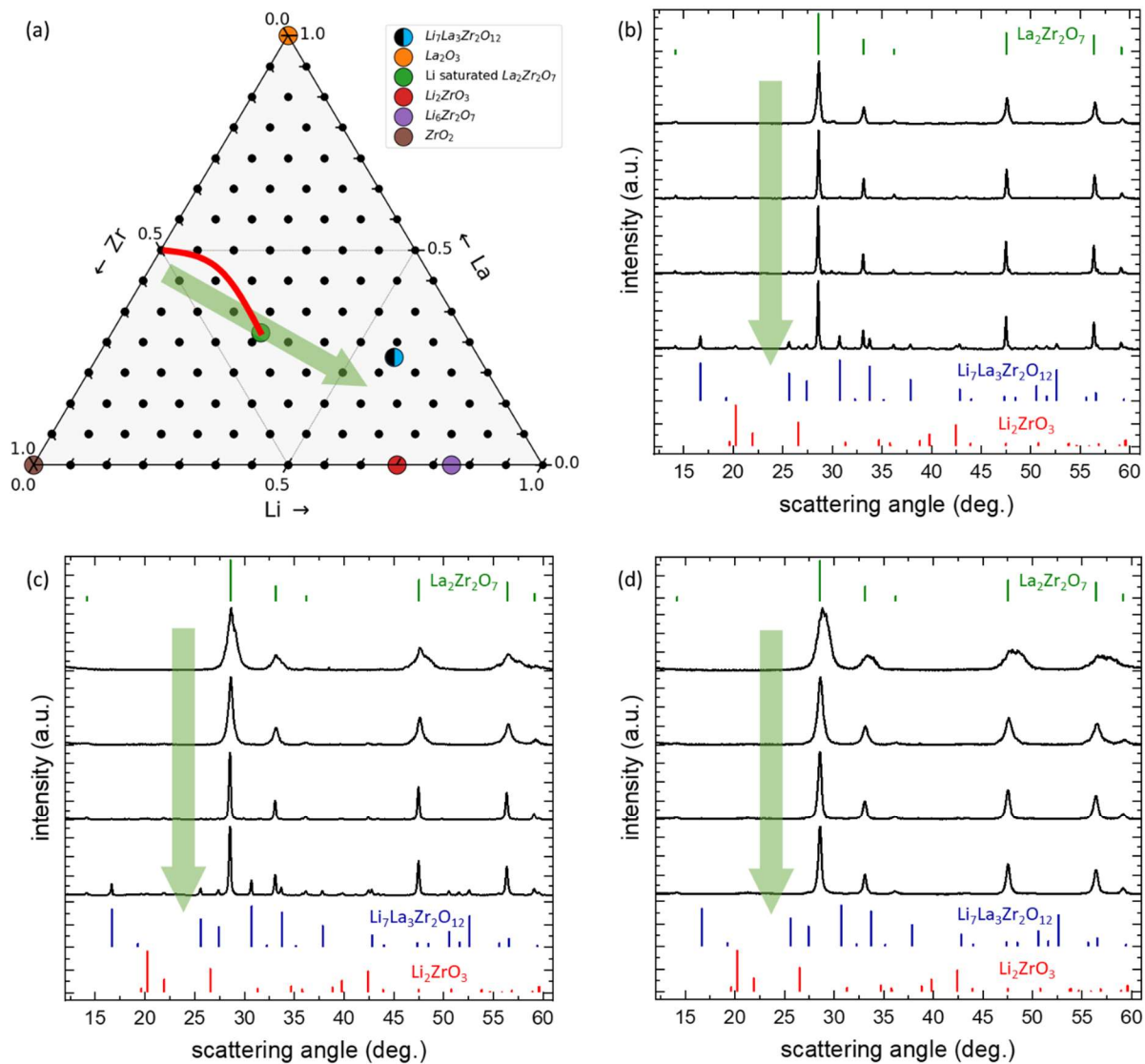


Figure 6: Pseudoternary diagram obtained at 900 °C (a) with a composition line indicating samples yielding PXRD patterns shown in the other panels. The synthesis temperatures were 900 °C (b), 800 °C (c) and 700 °C (d). Relevant reference patterns are also shown.

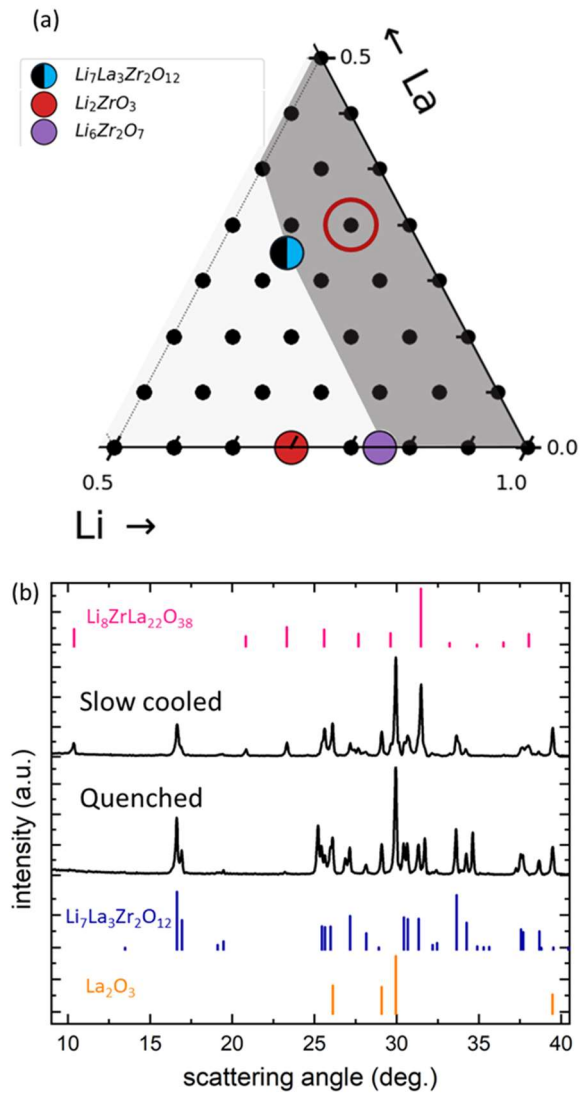


Figure 7: Partial pseudoternary diagram (a) indicating a composition in the red circle where a metastable phase was present during regular cooling. (b) Comparison of PXRD patterns of quenched and regular cooled samples after heating to 900 °C at the composition showing the metastable phase (peaks indicated by *).

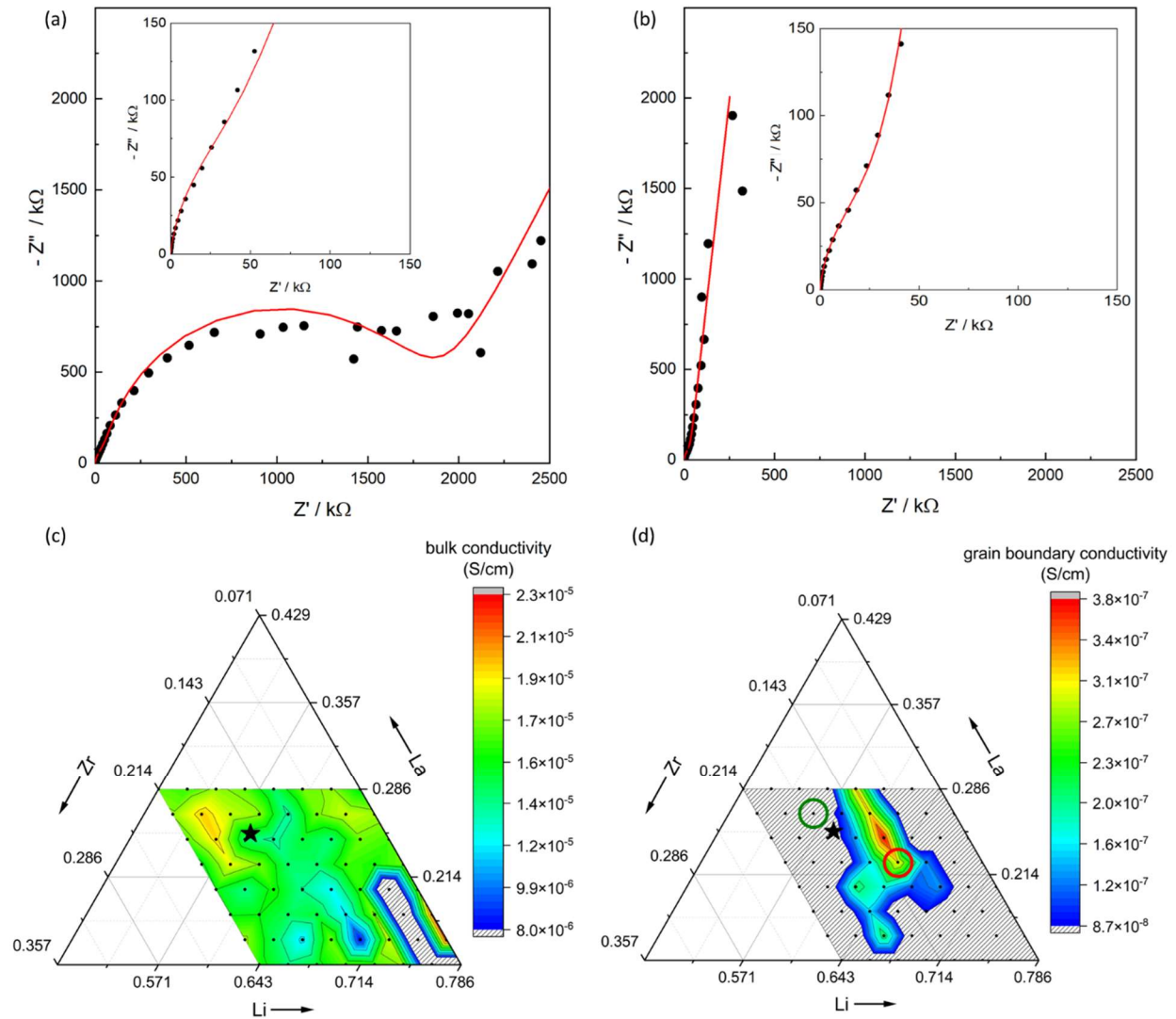


Figure 8: EIS spectra of both high total conductivity (a) and low total conductivity (b) samples of $\text{Li}_7\text{La}_3\text{Zr}_2\text{O}_{12}$. Heat maps of bulk (c) and grain boundary (d) ionic conductivities in the $\text{Li}_7\text{La}_3\text{Zr}_2\text{O}_{12}$ region (the actual composition of $\text{Li}_7\text{La}_3\text{Zr}_2\text{O}_{12}$ is indicated by a *). Compositions in (a) and (b) are indicated by the red and green circles in (d), respectively. Greyed-out compositions in (d) indicate a grain boundary conductivity too low to be reliably measured. Greyed out compositions in (c) represent spectra that were not recorded. All samples here were synthesized at 900 °C.